Removal of Na^+ and Ca^{2+} with Prussian Blue Analogue Electrodes for Brackish Water Desalination

Elias Sebti,[a] Münir M. Besli,[b,c] Michael Metzger,[b] Sondra Hellstrom,[b] Morgan J. Schultz-Neu,[a] Judith Alvarado,[a] Jake Christensen,[b] Marca Doeff,[a] Saravanan Kuppan,[b,*] Chinmayee V. Subban[a,*]

[a] Energy Storage and Distributed Resources Division, Lawrence Berkeley National Laboratory, Berkeley, CA 94720, USA

[b] Robert Bosch LLC, Research and Technology Center, Sunnyvale, CA 94085, USA

[c] Department of Mechanical Engineering, Karlsruhe Institute of Technology (KIT), Karlsruhe 76131, Germany

*Correspondence and requests for materials should be addressed to S.K.(Saravanan.Kuppan@us.bosch.com) and C.V.S (cvsubban@lbl.gov)

Abstract

Desalination of brackish water sources is critical to addressing the growing global freshwater demand. One promising approach is electrically driven desalination using intercalation electrodes. While intercalation electrodes have been widely researched for energy storage applications, only a small subset of those materials is suitable for desalination. Here we report the synthesis, characterization, and in-device testing of three Prussian blue analogue intercalation compounds: copper, manganese, and zinc hexacyanoferrate with formulas $K_xM[Fe(CN)_6]_z \cdot nH_2O$ (M = Cu, Mn, Zn). The desalination performance for each of these materials against carbon electrodes is reported for Na^+ intercalation and for Ca^{2+} intercalation using 1000 ppm NaCl and 1000 ppm $CaCl_2$ feed solutions respectively. While the copper and manganese analogs showed promising performance for Na^+ and Ca^{2+} intercalation, the zinc compound was unstable and underwent rapid dissolution. Manganese hexacyanoferrate showed the best desalination performance in terms of salt removal capacities and salt removal rates with NaCl while copper hexacyanoferrate performed the best with $CaCl_2$. The manganese analog proved to be the most stable intercalation material, retaining 83% and 72% of its salt removal capacity after 280 cycles in NaCl and $CaCl_2$ feed solutions respectively.

Key words

Brackish water, desalination, intercalation, Prussian blue analogue, Na-ion, Ca-ion

1. Introduction

Climate change and population growth have led to growing freshwater shortages around the world [1,2]. Sustainably meeting the increased freshwater demand requires a comprehensive approach, one that includes desalination. In particular, the desalination of widely available low-salinity brackish water sources is valuable as it allows for distributed water treatment, a feature considered critical for next generation water infrastructure [3].

There are several commercial desalination technologies available today, which operate based on either thermal, membrane, or electrical separation. Among them, calculations suggest thermal desalination is the most energy-intensive, irrespective of source water salinity. Electrically driven salt-separation approaches are predicted to be more energy-efficient than membrane-based methods such as reverse osmosis (RO) for low-salinity, brackish water sources [4]. Besides desirable energy efficiency, electrically driven technologies also tend to have higher freshwater recovery rates (85–90%) than either RO (25–80%) or typical thermal technologies (35%) [5–7]. Commercially

available electrically driven desalination technologies include electrodialysis (ED) and membrane capacitive deionization (mCDI). ED relies on expensive membranes prone to fouling [8], while mCDI technology is limited by carbon electrode capacities and lifetime [9,10]. Hence, there is a need for developing new approaches towards electrically driven brackish water desalination.

Ideal electrodes for electrically driven desalination must be non-toxic, inexpensive, electrochemically stable, able to remove a wide range of ions, and have high salt-capture capacities. Such desirable characteristics as high capacities at moderate applied voltages and potential for ion selectivity make intercalation electrodes a promising option for brackish water desalination [11]. Intercalation materials operate by exclusively inserting cations into lattice sites using the same principles underlying most modern Li-ion battery technology. The intercalation mechanism helps reduce co-ion expulsion, a deleterious effect in capacitive deionization where ions of the same charge as the applied voltage are repelled from the electric double layer, in the absence of membranes or surface modifications. Although intercalation electrodes have been extensively researched for Li-ion and Na-ion batteries [11,12], due to the low operational voltage limit (<1.23 V) in aqueous environments, only a subset of the reported compounds is suitable for desalination. One such promising family of materials are metal organic frameworks (MOFs) known as Prussian blue (PB) and Prussian blue analogues (PBA) [13]. PBAs are cyano-bridged compounds of the general formula $A_xM_A[M_B(CN)_6]_z \cdot nH_2O$, where M_A and M_B are transition metals (Mn, Fe, Co, Ni, Cu, or Zn) and A is an alkali metal (Li, Na, or K), with large three-dimensional diffusion channels (~5 Å) that facilitate ion intercalation/deintercalation [14]. PBAs are also readily available and inexpensive (≈$5/kg) [12], making them good candidates for scale-up of intercalation desalination technologies.

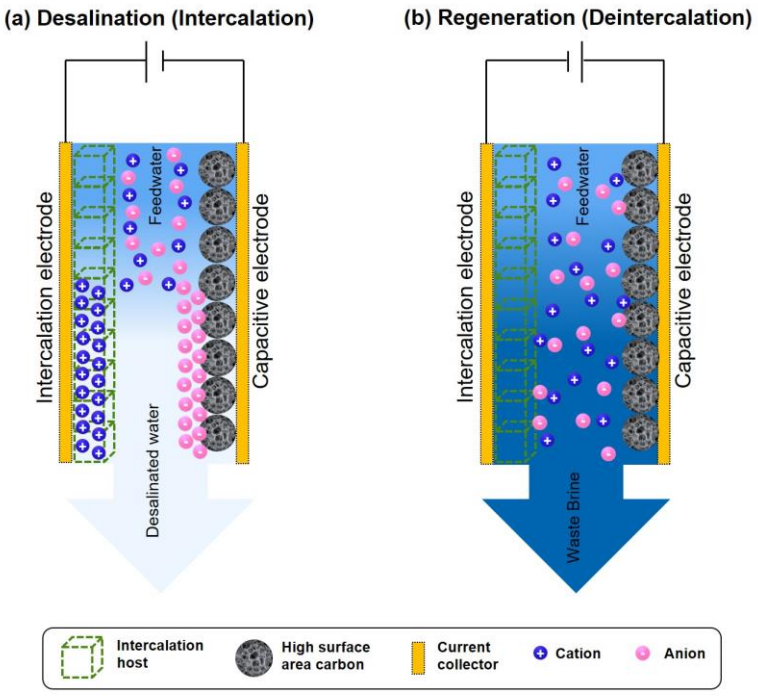

Figure 1. Schematic showing intercalationbased desalination (a) and subsequent deintercalationbased regeneration (b). Cations are captured by the intercalation host (left electrode) while anions are adsorbed onto the carbon electrodes (right electrode).

Various PBAs have been tested as cathodes for Li-ion, Na-ion, and Ca-ion batteries [15–17]. A subset of them have also been studied for desalination[18,19]. Prior reports on the use of PBAs for desalination has been demonstrated using different system configurations achieved by coupling different salt removal mechanisms: purely intercalation-

based deionization[20,21], intercalation electrode paired with a conversion electrode[22], and intercalation electrode paired with a capacitive electrode[23]. While most studies have focused on flow-by electrode configurations, there are also reports on desalination with PBA electrodes in the flow-through configuration[24,25]. Given the existing body of literature on Prussian blue and Ni-containing PBA (NiHCF), our work is focused on PBA materials that are relatively less studied for desalination applications. In this study, we report the synthesis, characterization, and in-device desalination performance of three PBAs with a general formula of $K_xM[Fe(CN)_6]_z \cdot nH_2O$, where M is Cu, Mn, or Zn. We refer to the compounds as CuHCF, MnHCF, and ZnHCF and test their desalination performance using a hybrid cell concept (Figure 1), where cations are captured by PBA electrodes through intercalation and anions are captured on carbon electrodes via adsorption. We use a flow-by cell configuration. While CuHCF has been widely studied for desalination [11,26,27], the use of ZnHCF [28,29] and MnHCF [13–15] has been mostly limited to energy storage applications. To the best of our knowledge, this is the very first report on the use of MnHCF and ZnHCF for desalination. A recent study also looked at CuHCF, MnHCF, NiHCF, and ZnHCF materials for salinity gradient energy recovery application [30]. However, most prior reports on the use of PBAs for desalination are focused on Na^+ intercalation [11], with a couple recent studies evaluating divalent cation intercalation in aqueous electrolytes [31–33]. While low to intermediate salinity (1,000 to 10,000 ppm) is a characteristic feature for brackish sources (vs. 35,000 ppm of seawater), the exact ionic composition can be highly variable from one source to the next [34]. Such compositional variability makes effective brackish water desalination a challenge today. Given that most brackish sources contain a mixture of monovalent and divalent ions, the ability to intercalate both types of ions is advantageous for effective desalination. This is particularly true for Ca^{2+} ions, which cause electrode scaling and, as a result, decrease overall electrode lifetime. Therefore, in order to identify suitable electrodes for brackish water treatment, we explored both Na^+ and Ca^{2+} intercalation into each of the PBA electrodes using 1000 ppm solutions of NaCl or $CaCl_2$. Our results show promising and reliable salt removal upon continuous cycling for 125h with CuHCF and MnHCF for both Na^+ and Ca^{2+} intercalation, with the higher salt removal capacity observed in the Mn compound.

2. Experimental Section

2.1 Materials Synthesis

$K_xM[Fe(CN)_6]_z \cdot nH_2O$ (K-MHCF) powder, where M is Cu, Mn and Zn, was synthesized by co-precipitation with slight modifications to previously reported methods [35]. 100 mL of 0.05 M $K_3Fe(CN)_6$ and 0.1 M MCl_2 (M = Cu, Mn and Zn) aqueous solutions were added dropwise (1 mL/min, over 1.4 h) simultaneously into 100 mL of DI-water under vigorous stirring (500 rpm) at room temperature. The as-obtained precipitates were filtered and washed with copious amounts of water. Finally, the washed precipitates were dried overnight at 60°C.

2.2 Materials Characterization

X-ray diffraction: Powder X-ray diffraction patterns were recorded using a Bruker D8 ADVANCE X-ray diffractometer equipped with a Cu K-α radiation source. The accelerating voltage and current were 40 kV and 40 mA, respectively. Scans were performed between 10 and 60° (2Θ) at a scan speed of 0.02°/s and a step size of 0.01°. Lattice parameters and phase ratios were determined using full-pattern Rietveld refinements using FullProf Suite®.

Microscopy and Elemental Analysis: Scanning electron microscopy (SEM) imaging and energy dispersive X-ray spectroscopy (EDS) were conducted using a JEOL JSM-7200F Field Emission Scanning Electron Microscope equipped with an Oxford X-Max^N 50 Silicon Drift Detector system. SEM imaging was performed using an accelerating voltage of 5 kV at medium probe currents using the secondary electron detector. EDS was conducted using an accelerating voltage of 20 kV at high probe currents.

Synchrotron soft X-ray absorption spectroscopy: A thin layer of each sample was spread onto a conductive carbon tape which was then attached to an aluminum sample holder. Measurements for K-edge and L-edge were carried out at the 31-pole wiggler beamline 10-1 of the Stanford Synchrotron Radiation Lightsource (SSRL) using a spherical grating monochromator with 20 mm entrance and exit slits, a 0.2 eV energy resolution and a 1 mm^2 beam spot. Data were collected at room temperature under ultrahigh vacuum (10^{-9} Torr) in a single load, simultaneously using the total electron yield (TEY) and fluorescence yield (FY) mode detectors. Obtained spectra were then normalized to the incident flux.

Inductively coupled plasma—optical emission spectrometry (ICP-OES): The CuHCF, MnHCF, and ZnHCF samples were weighed and transferred into Pyrex glass beakers. 3 ml of conc. hydrochloric acid (HCl, trace metal grade, 35-38 wt%, Fischer Scientific), 2 ml of conc. nitric acid (HNO_3, trace metal grade, 65-70 wt%, Fischer Scientific), and a squirt of deionized water were subsequently added. The mixtures were heated on a hot plate at 250 °C to complete visible digestion, then diluted with deionized water to reach an appropriate concentration range for subsequent analysis by ICP-OES (iCAP 7400 Radial, Thermo Fischer Scientific, USA). Quantification was performed using external six-point calibration ($R^2 > 0.9999$) with multi element standards ranging from 1, 5, 10, 20, 50, and 100 µg/ml in a 5% v/v HNO_3 matrix (Inorganic Ventures, USA). Operating conditions for the ICP-OES measurements included nebulizer gas flow of 0.62 L/min, coolant gas flow of 12 L/min, and the auxiliary gas flow of 0.5 L/min, and RF power of 1150 W.

2.3 Electrode Fabrication

Each MHCF electrode was prepared by mixing 80% by weight of the synthesized active material, 10% by weight polyvinylidene difluoride (PVDF, Kynar HSV 900), and 10% by weight conductive carbon black (TIMCAL Super P- Li) in N-methylpyrrolidone (NMP, Sigma Aldrich). The mixture was stirred for two hours with a homogenizer (at 3000 rpm) in an argon-filled glovebox (UNIlab Pro, MBRAUN) to prepare a viscous slurry. The slurry was then spread onto the surface of a graphite current collector (Ceramaterials, 250 µm thick) which was calendared to achieve flat and uniform thickness (approximately 200 µm) prior to coating. A metallic current collector was not used to avoid corrosion. The printed electrode was allowed to dry for two days at room temperature inside the glovebox. Upon fully drying, the electrode thickness was measured and a 9 cm x 10 cm electrode was cut from the coated electrode sheet for in-device testing. The active material loadings and electrode thicknesses for each MHCF material are provided in Table S4. A carbon counter electrode of the same dimensions was cut from a piece of commercial carbon nanofoam paper (Grade II, Marketech, 250 µm thick). The carbon electrodes had a reported BET surface area of 600 m^2/g and were composed of 87% nanoporous carbon and 13% carbon fiber by weight. The active material loading for the carbon electrode was 10.4 mg/cm^2. Both electrodes were inserted into a custom-built flow cell (see supplementary information Figure S1) and an electrically insulating nylon mesh separator (WN0250, Industrial Netting, 250 µm thick) was inserted between them. Control experiments were conducted using carbon nanofoam electrodes for both the anode and cathode in the same flow cell and keeping all other parameters the same.

2.4 Desalination Performance Testing

A custom test setup (Figure 2, Figure S1) capable of collecting continuous, in-line data was used to test the desalination performance of the MHCF materials. Automation of the test setup and data acquisition was achieved using commercial hardware and custom software. A DC power supply (Keithley 2401 SourceMeter) was used to control the voltage cycling of the cell and to measure the current drawn, and a peristaltic pump (Masterflex L/S) was used to continuously pump feedwater from an 80 L reservoir through the cell at 10 mL/min. Both conductivity and pH were measured with in-line probes (Vernier) before and after the flow cell.

The desalination performance of each MHCF material was tested with two different feed solutions: 1000 ppm NaCl (17 mM) and 1000 ppm $CaCl_2$ (9 mM). The testing protocol sampled a variety of symmetric cycling times ranging

from 4 to 60 minutes (for the full cycle), and the complete test protocol lasted 125h (details in Table S1), which included 250 standard cycles (20 min each) and 10 long cycles (60 min each). The longer cycles were conducted at regular intervals during the test protocol to evaluate electrode capacity retention with cycling. MHCF/carbon and symmetric carbon/carbon cells were both tested using the same protocol but in slightly different voltage windows. The intercalation-based MHCF/carbon systems were cycled between +1 V and –1 V applied potential, while the adsorption-based carbon/carbon cells were cycled between –1 V and 0 V. The symmetric carbon cell was shorted during discharge to avoid re-adsorption of ions that occurs with voltage polarity reversal. The MHCF systems were not subject to this issue as the anions cannot be intercalated into the structure. A significantly higher active material loading on the carbon electrode was used to ensure that the intercalation electrode would be the limiting electrode.

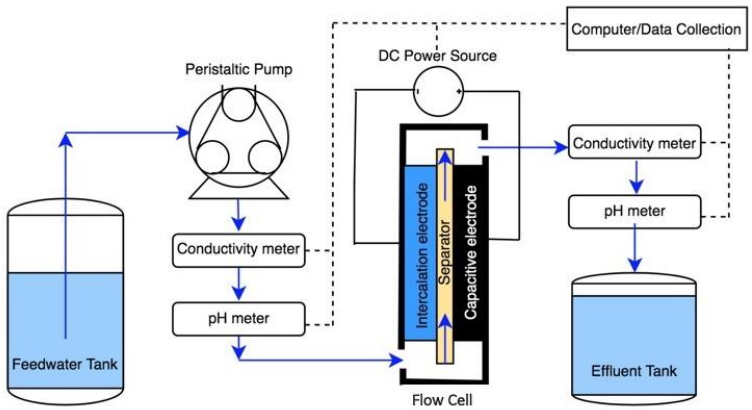

Figure 2. Process flow diagram of the experimental setup. In-line conductivity and pH meters were used for continuous monitoring of feedwater and effluent water quality and a DC power supply was used for voltage cycling and current measurements. Photographs of the setup and the prototype device are provided in Figure S1.

2.5 Data Analysis

To quantify the desalination performance of each material, conductivities of both the influent and effluent streams were monitored throughout each test. Salt concentration was calculated directly from raw conductivity data using the following three-point linear calibration models:

$$C_{NaCl} = 0.5193 * \sigma - 31.55 \qquad C_{CaCl_2} = 0.5141 * \sigma \ - 36.59$$

where σ is the conductivity of the solution (in µS/cm) and C_{NaCl} and C_{CaCl_2} are the concentrations of NaCl and $CaCl_2$ (in ppm), respectively. The influent concentration was subtracted from the effluent concentration to calculate changes in salt concentration; these were then integrated to obtain the salt removal capacity (SRC) of a given material. While many researchers refer to this metric as the salt adsorption capacity (SAC) [36], SRC is used in this work as a more general term for comparing systems that rely on adsorption as well as intercalation. The SRC is calculated as follows:

$$SRC = (\int_{cycle\ start}^{t} f * \Delta C_s * dt)/m_{AM} \qquad (1)$$

where f is the flow rate (in L/s), ΔC_s is the change in salt concentration (in g/L), and m_{AM} is the mass of active material in the cathode (in g). The m_{AM} values were also used to obtain normalized performance data. For intercalation systems (MHCF/carbon), this corresponded to the mass of active material (MHCF) and for adsorption

systems (carbon/carbon), the mass of high surface area carbon. The salt removal rate (SRR) for each material is calculated as the derivative of its SRC with respect to time. Coulombic efficiency (CE), another key performance metric, was calculated using equation (2):

$$CE = 100 * (\int_{discharge\ start}^{discharge\ end} I * dt)/(\int_{charge\ start}^{charge\ end} I * dt) \qquad (2)$$

where I is the current through the cell. Discharge cycles correspond to electrode regeneration steps (deintercalation/desorption) and charge cycles correspond to desalination steps (intercalation/adsorption). Charge efficiency (Λ), the ratio of removed salt to charge transferred for charge cycles, was calculated using equation (3):

$$\Lambda = (Z * m_s/M_W)/((\int_{charge\ start}^{charge\ end} I * dt)/F) \qquad (3)$$

where Z is the number of electrons transferred to the cation, m_s is the total mass of salt removed in a cycle, M_W is the molar mass of the salt, I is the current through the cell, and F is Faraday's constant (96,485 C/mol). Because of the difference in applied voltages for discharge between MHCF/C and C/C systems, Λ was only assessed for charge cycles. Finally, energy per ion (EPI) consumption (in kT) was calculated according to equation (4):

$$EPI = (M_W/(n * m_s)) * (\int_{charge\ start}^{charge\ end} E_{cell} * I * dt)/(RT) \qquad (4)$$

where n is the number of ions per salt molecule, E_{cell} is the applied potential, R is the ideal gas constant (in J/mol*K), and T is room temperature (298 K).

3. Results and Discussion

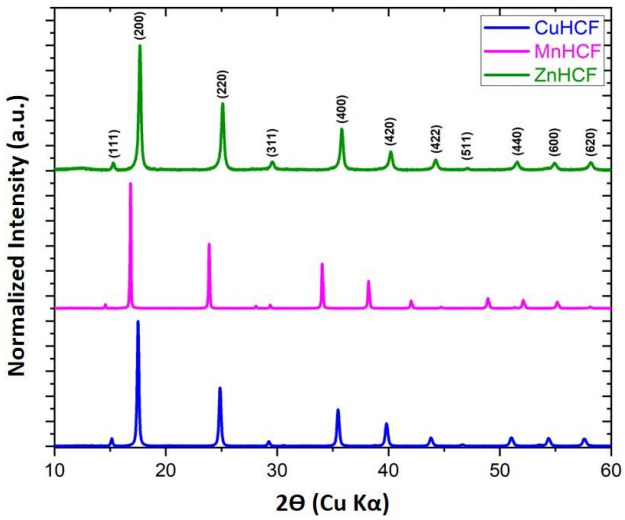

Figure 3. Powder X-ray diffraction patterns for each MHCF pristine electrode powder along with Miller indices for all reflections.

Figure 3 shows the normalized room temperature powder X-ray diffraction (XRD) pattern of the as-synthesized samples. All three MHCFs (M = Cu, Mn and Zn) crystallize in the face-centered cubic structure (FCC, space group: $Fm\bar{3}m$) with high crystallinity and phase purity. In general, the structure of PBAs, $K_xM[Fe(CN)_6]_y \cdot zH_2O$ (M = transition metal, x = 4y–2, y ≤ 1), feature a rigid cubic framework of linear −Fe−C−N−M− chains; $Fe^{2+/3+}$and $M^{2+/3+}$ reside on alternate corners of 8 sub cubes of corner-shared octahedra (4a and 4b positions) coordinated to −CN and −NC groups, respectively in the FCC unit cell ($Fm\bar{3}m$, Z = 4). Rietveld refinement of the lattice parameters (Figure S5) yields unit-cell lengths of *a* = 10.1137 Å, *a* = 10.5316 Å, and *a* = 10.3482 Å for CuHCF, MnHCF and ZnHCF, respectively, which is in good agreement with previous reports [37,38]. The molar ratios between the K, M and Fe of the MHCF materials were examined by ICP-OES, and their stoichiometric compositions were determined to be $K_{0.04}Cu[Fe(CN)_6]_{0.68}$, $K_{0.06}Mn[Fe(CN)_6]_{0.65}$, and $K_{0.03}Zn[Fe(CN)_6]_{0.65}$.

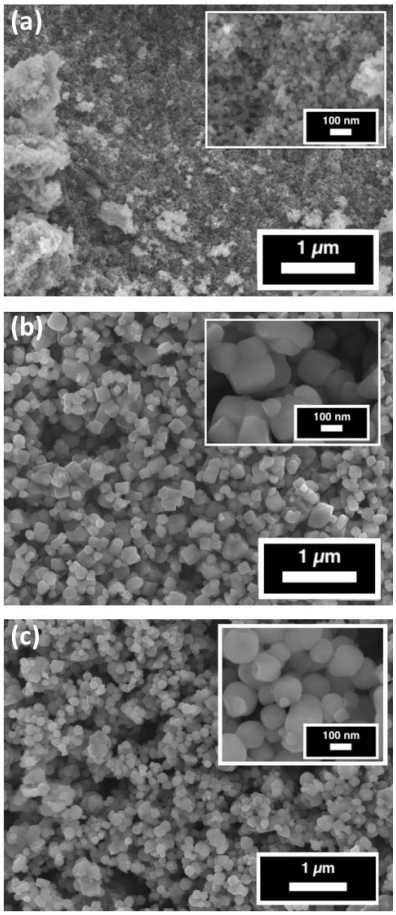

Figure 4. SEM images of (a) CuHCF, (b) MnHCF, and (c) ZnHCF pristine electrode powders. Insets show higher magnification images to highlight average particle size.

SEM investigation (Figure 4) of as synthesized K-MHCF samples revealed varying morphologies. The CuHCF crystallized as irregular shaped nanoparticles (30-40 nm), MnHCF crystallized as cube shaped nanoparticles (100-300 nm), while the ZnHCF formed spherical shaped particles (100-300 nm).

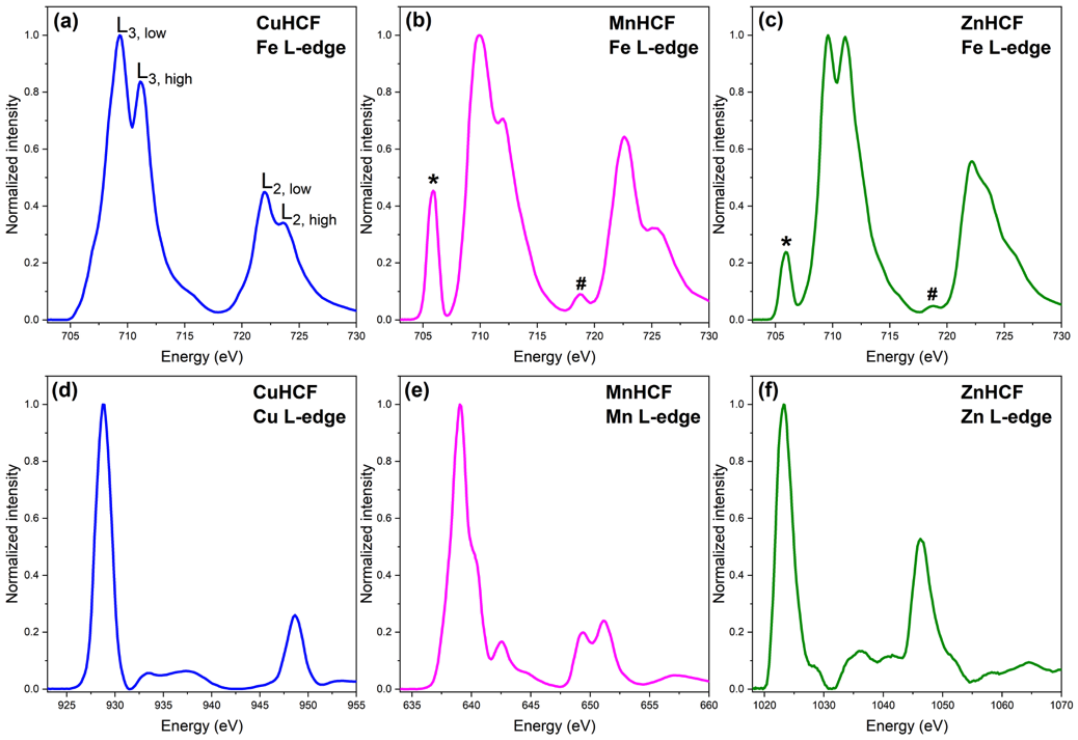

Figure 5. Soft X-ray absorption spectroscopy data obtained in transmission mode for pristine CuHCF, MnHCF, and ZnHCF. (a-c) Fe L-edge spectrum for CuHCF, MnHCF, and ZnHCF, respectively. In panels (b) and (c), peaks at 706.0 and 718.8 eV (labeled with an * and # respectively) indicate the presence of Fe^{3+}. The Cu L-edge (d), Mn L-edge (e), and Zn L-edge (f), indicate an oxidation state of 2+ for the transition metals.

Transition metal (TM) L-edge soft X-ray absorption spectroscopy (soft XAS) has been extensively applied to analyze various materials in the field of biology, materials science as well as energy technology [39,40]. In comparison to X-ray absorption near edge structure (XANES) spectroscopy, which probes the excitation of electrons from core levels into unoccupied energy levels and offers bulk-sensitive information, soft XAS yields information on the 3d states and is surface-sensitive. The penetration depth of soft X-rays can be very low and, depending on the mode of detection, one can get information from 1-2 nm (auger electron yield, AEY), 5 nm (total electron yield, TEY), or 50-100 nm depth (fluorescence yield, FY). The TM L-edge absorption spectrum can be separated into two main regions due to spin-orbit interaction of the core hole, namely L_3 and L_2, which correspond to the transitions from $2p_{2/3}$ and $2p_{1/2}$ into 3d orbitals, respectively [41]. Additional splitting of each edge is due to crystal field effects and 2p-3d interactions [42].

Figure 5 shows the Fe L-edge and corresponding transition metal L-edge spectra for CuHCF, MnHCF, and ZnHCF. While the L-edges of Cu, Mn, and Zn (Figure 5d-f) all indicate a valence state of 2+, the Fe L-edges for the corresponding MHCFs shows slight differences. The double peaks centered at approximately 710 and 722 eV are visible in all of the Fe L-edge measurements (Figure 5a-c) and are associated with a 2+ valence state. MnHCF and ZnHCF (Figure 5b-c) both show clear Fe^{3+} peaks at 706.0 and 718.8 eV indicating the presence a valence state of 3+ for Fe, which is in agreement with the literature [43,44]. In contrast, the CuHCF (Figure 5a) only shows a small peak at 718.8 eV and the Fe^{3+} peak at 706.0 eV is hidden by the much broader L_3 peak, indicating that most of the iron in CuHCF exists as Fe^{2+}, unlike MnHCF and ZnHCF. In summary, all three samples have mixed valences for Fe, with Fe more oxidized in MnHCF and ZnHCF than in CuHCF. No significant difference is observed between the C and N K–edge of the different MHCFs (Figure S6).

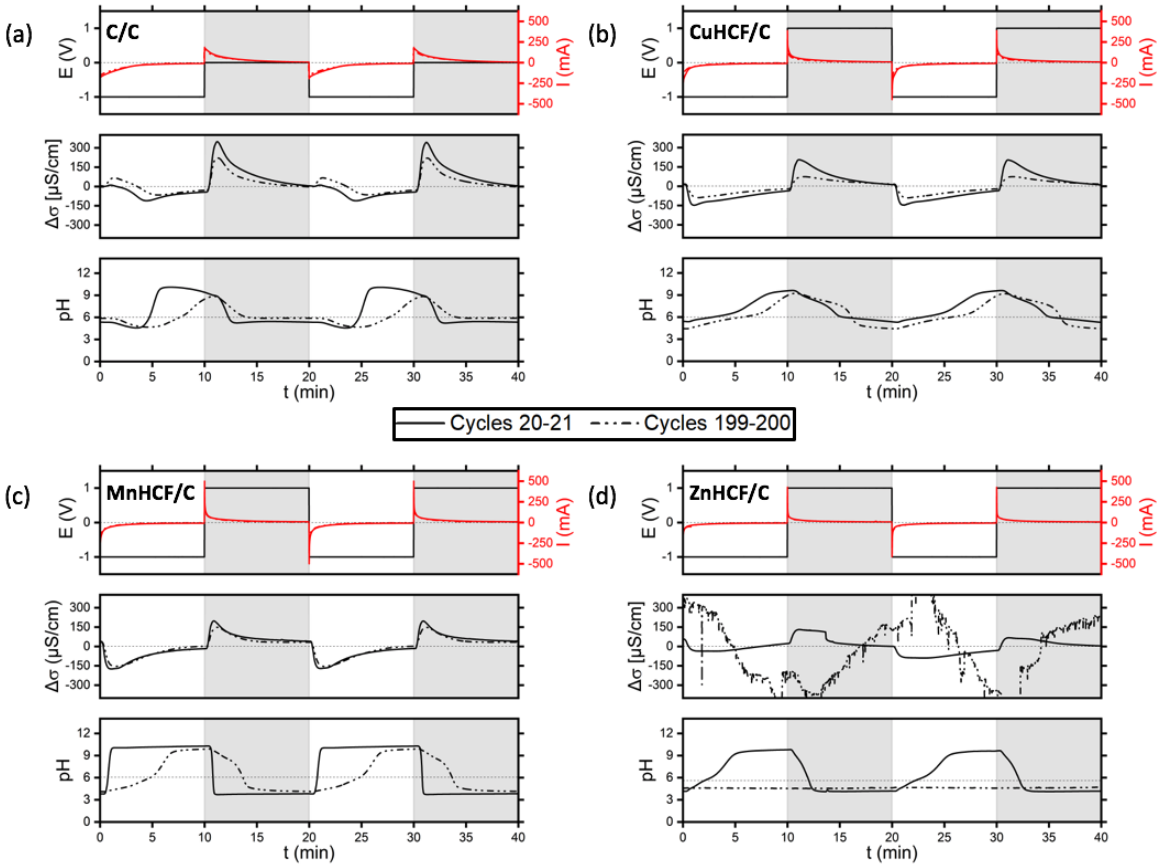

Figure 6. Current (I), voltage (E), change in conductivity (Δσ), and pH data for two consecutive salt-capture and salt-release cycles conducted with 1000 ppm NaCl feedwater: (a) C/C, (b) CuHCF/C, (c) MnHCF/C, and (d) ZnHCF/C systems. For the MHCF/C systems, each cycle was 10 min at –1 V followed by 10 min at +1 V, and for the C/C system it was 10 min at –1 V followed by 10 min at 0 V. Early cycles (solid lines) correspond to the 20th and 21st cycles while later cycles (dashed lines) correspond to the 199th and 200th cycles. The deintercalation (salt release) stage of each cycle is shown with grey background fill. The grey dotted line in the pH panels is the pH of the feedwater.

Figure 6 displays results from the desalination performance tests for the symmetric C/C and each of the MHCF/C systems conducted with 1000 ppm (17 mM) NaCl feedwater. Current-voltage, conductivity, and pH data from two sets of identical cycles are displayed in each panel, one set from the early (cycles 20-21) and one from the later stages (cycles 199-200) of the 10 min charge/10 min discharge test protocol. These cycles were at steady-state, meaning that the performance exhibited in Figure 6 was unchanged for an extended period of time within the same series of cycles. The continuous cycling of the symmetric carbon electrodes showed significant decline in the desalination performance, as evidenced by the decrease in the peak magnitudes for Δσ between early and later stages (middle panel, Figure 6a). Further, with continuous cycling, an inversion effect was observed where Δσ increased despite an applied potential—a result of simultaneous trace oxygen reduction and desorption of co-ions dominating counter-ion adsorption[45]. Changes observed in the pH behavior upon continuous cycling of the C/C system can be attributed to widely reported parasitic side reactions occurring at the carbon surface [9,10,46–52]. In Figure 6b, the CuHCF/C system showed promising performance in early stages but significantly degraded with cycling. While the corresponding current profiles for the early and late cycles do not appear dramatically different, the Δσ profile flattens out for the aged electrode, suggesting an increase in side reactions and a decrease in electrode capacity. This performance decrease in CuHCF/C is believed to be a result of both mechanical loss and chemical

leaching of the active material from the cathode. Evidence of chemical dissolution of active material [53] was observed in the form of copper oxide deposits on the separator and carbon counter electrode upon opening the cell post-cycling (Figure S7). With cycling, pH fluctuations were also observed in the CuHCF/C system. While the pH behavior did not change drastically with continuous cycling (i.e. no change in curve shape), the pH curves were temporally offset from applied voltage, shifting forward in time, suggesting a correlation between the rate of pH change and electrode aging. The MnHCF/C system appears to retain its capacity (Figure 6c) upon cycling. The Δσ profile for later stage cycling of MnHCF/C closely mirrors that for early stages, highlighting electrode robustness. However, the corresponding pH profiles differ significantly, with early cycling displaying square-profile curves and later cycling displaying more rounded-profile curves that are shifted forward in time. Finally, the ZnHCF/C system (Figure 6d) proved to be highly unstable upon cycling. The early cycles show some salt removal (negative Δσ values) during charging but later cycles suggest the system no longer functions, as indicated by the Δσ profile losing its characteristic shape and the pH profile reaching a flatline. As in the CuHCF/C system, dissolution of active material was observed with ZnHCF/C. In this case, the effluent tank turned green from the presence of loose electrode material and white ZnO deposits were discovered on the carbon electrode surface during postmortem analysis (Figure S7). These results are in agreement with a previous study that reported dissolution and instability of ZnHCF in aqueous Na_2SO_4 electrolytes [29].

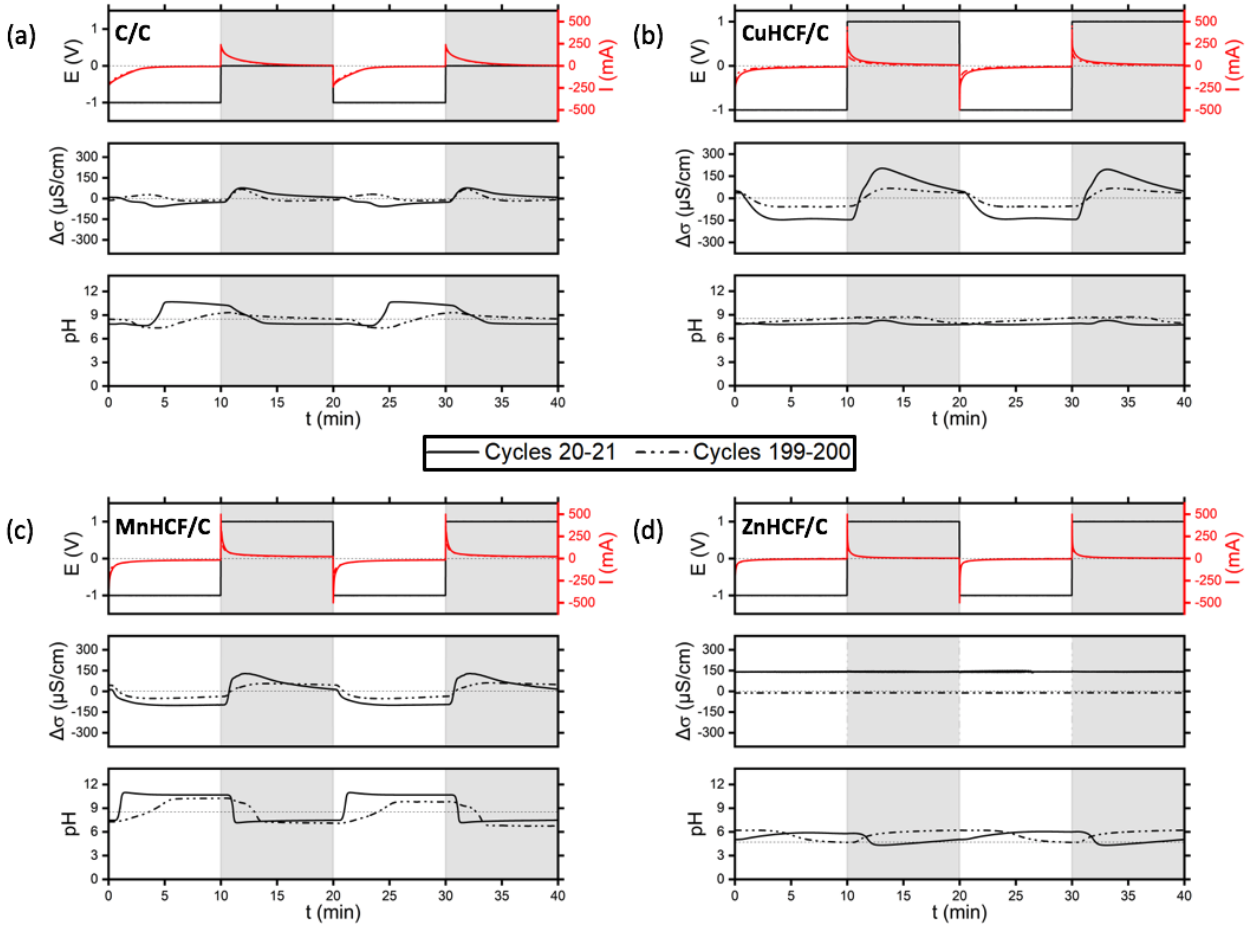

Figure 7. Current (I), voltage (E), change in conductivity (Δσ), and pH data for two consecutive salt-capture and salt-release cycles conducted with 1000 ppm $CaCl_2$ feedwater: (a) C/C, (b) CuHCF/C, (c) MnHCF/C, and (d) ZnHCF/C systems. For the MHCF/C systems, each cycle was 10 min at –1 V followed by 10 min at +1 V, and for the C/C system it was 10 min at –1 V followed by 10 min at 0 V. Early cycles (solid lines) correspond to the 20th and 21st

cycles while later cycles (dashed lines) correspond to the 199th and 200th cycles. Deintercalation (salt release) stage of each cycle is shown with grey background fill. The grey dotted line in the pH panels is the pH of the feedwater.

Figure 7 displays the results of desalination performance tests for C/C and MHCF/C systems conducted with 1000 ppm (9 mM) $CaCl_2$ feedwater. For the symmetric C/C system (Figure 7a), cycling with $CaCl_2$ yielded a similar Δσ and pH profile to NaCl tests but with lower magnitude peaks. With continuous cycling, a decrease in the magnitude of the Δσ maxima and minima was observed for the CuHCF/C (Figure 7b) and MnHCF/C (Figure 7c) systems, suggesting a decrease in electrode capacity for both materials. However, changes to their pH profiles upon continuous cycling were significantly different, with the CuHCF/C system showing very small pH oscillations compared to the MnHCF/C system. The larger pH oscillations in MnHCF/C showed similar profiles to those observed in the C/C system, suggesting that the pH behavior in these cases could be linked to undesirable side reactions at the carbon anode. As with the NaCl tests, the ZnHCF/C (Figure 7d) system showed no desalination performance, failing to yield an oscillating Δσ profile. However, changes in pH were observed during cycling, which is likely due to a combination of electrode capacity mismatch and carbon oxidation. Post-mortem analysis of the electrodes showed clear signs of ZnHCF instability, with white zinc oxide deposits on the separator and carbon electrodes (Figure S7). Given the instability and rapid dissolution of ZnHCF in both NaCl and $CaCl_2$ feed solutions, the ZnHCF/C system was not further investigated.

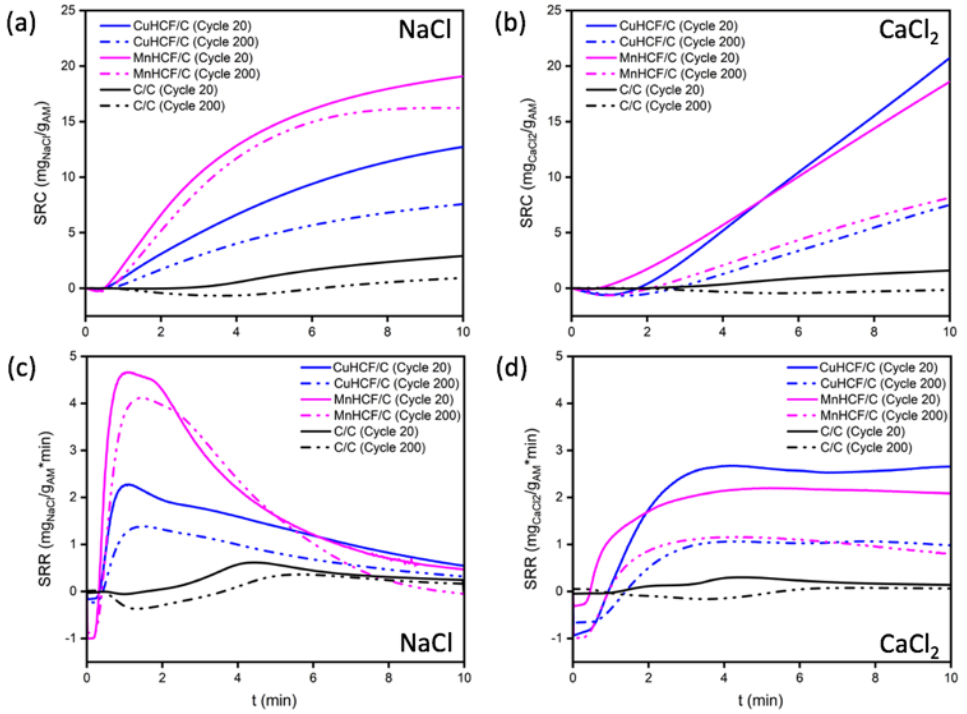

Figure 8. Salt removal capacity (a-b) and rate (c-d) calculated for the early and later desalination cycles of tests conducted with NaCl and $CaCl_2$ feedwaters. Each cycle consisted of symmetric 10 min salt-capture and salt-release steps (20 min full cycle). Early cycles (solid lines) correspond to the 20th cycle while later cycles (dashed lines) correspond to the 200th cycle.

The SRC and SRR were calculated for CuHCF/C, MnHCF/C, and symmetric C/C systems tested with 1000 ppm NaCl and 1000 ppm $CaCl_2$ feed solutions (Figure 8). These values were calculated using the raw data presented in Figure 6 and Figure 7. Values of SRC and SRR were normalized to the mass of active material in the electrode. The mass of active material was calculated using the weight of the cathode after fabrication and the wt% loading of active

material in it. Any loss of active material due to leaching and dissolution during testing could not be accounted for and is not included in our calculations. With NaCl feedwater (Figure 8a,c), the MnHCF/C system displayed the highest SRC for both the 20th and 200th cycles (19.1 and 16.2 mg/g_{AM}, respectively), retaining 85% of its capacity. In comparison, between the 20th and 200th cycles, CuHCF/C preserved only 60% of its SRC, going from 12.72 mg/g_{AM} to 7.57 mg/g_{AM}. MnHCF also removed NaCl the fastest, with more than double the rate observed in CuHCF. Finally, the C/C system had the lowest values for both SRC and SRR, but this is not a surprise given the higher electrode capacities expected for intercalation electrodes. At the 20th cycle, its SRC was 2.9 mg/g_{AM} and by the 200th cycle, that value was 0.9 mg/g_{AM}. In $CaCl_2$ feedwater (Figure 8b,d), neither the CuHCF/C nor the MnHCF/C system appears to reach saturation after charging (applying –1 V) for 10 min. CuHCF had a slightly higher SRC than MnHCF at the end of the 20th cycle (20.7 vs. 18.6 mg/g_{AM}), but was outperformed by MnHCF by the 200th cycle in $CaCl_2$ (7.5 vs. 8.1 mg/g_{AM}). The observed difference in SRC for MnHCF and CuHCF is negligible and is likely due to a decrease in SRR values rather than a decrease in total electrode capacity. Regardless of the feedwater composition or cycle number, MnHCF's SRR reached positive values before that of CuHCF, signifying that MnHCF had a shorter response time to an applied voltage and began desalinating faster during the charging step. Understanding selectivity for Na^+ vs. Ca^{2+} intercalation in MHCF/C systems requires additional experiments using complex feedwater matrices, but based on a recent study of monovalent and divalent cation selectivity in NiHCF [32], there is likely to be a preference for monovalent cations.

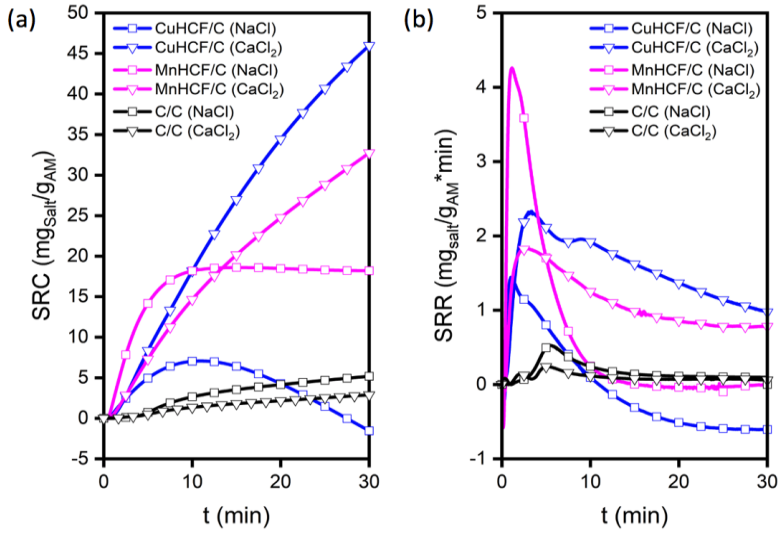

Figure 9. Salt removal capacity (a) and rate (b) for the first 30 min intercalation cycle (applied voltage of –1 V) of C/C, CuHCF/C, and MnHCF/C obtained in NaCl and $CaCl_2$ feedwaters.

To assess the full capacity of each system, 30 min charge (–1 V) and 30 min discharge (+1 V) cycles were performed at regular intervals as part of the test protocol. Results from the first such cycle are shown in Fig 9. When tested with NaCl feedwater, CuHCF/C, MnHCF/C, and C/C systems reached SRC of 7, 19, 5 mg/g_{AM}, respectively. CuHCF/C, MnHCF/C, and C/C systems cycled with $CaCl_2$ feedwater (Figure 9a) showed SRC of 46, 33, and 3 mg/g_{AM}, respectively. Figure S12 represents the same data in units of moles of salt. In general, intercalation-based MHCF/C systems performed better than adsorption-based C/C systems for the removal of Ca^{2+} ions, as the SRC for both MHCF materials in $CaCl_2$ was higher than that for carbon-only electrodes. Electrodes reached saturation (SRR = 0) faster in the 1000 ppm NaCl feedwater (Figure 9b) than in 1000 ppm $CaCl_2$. This is likely due to a combination of differences in the molar concentration of the NaCl and $CaCl_2$ feed solutions and differences in the mobilities of hydrated Na^+ and Ca^{2+}ions. Even after 30 min of charging, MHCF systems had not reached saturation with $CaCl_2$ feedwater (i.e. SRR remained >0), suggesting a need for longer cycles to fully utilize the electrode capacity when capturing Ca^{2+} from

solution. In comparison, when MHCF electrodes were operated at longer cycle times in NaCl feedwater, the SRR of CuHCF decreased to negative values, subsequently leading to lower SRC, and the MnHCF/C system reached a steady state SRR of 0 after about 13 min. The capacity loss observed in CuHCF/C system is likely due to enhanced dissolution of active material from the electrode at longer cycle times. This limited stability makes the use of longer cycle times to reach higher capacities with CuHCF less practical. Given no such electrode dissolution was observed with MnHCF, the results of our tests suggest MnHCF to be more robust than CuHCF for desalination.

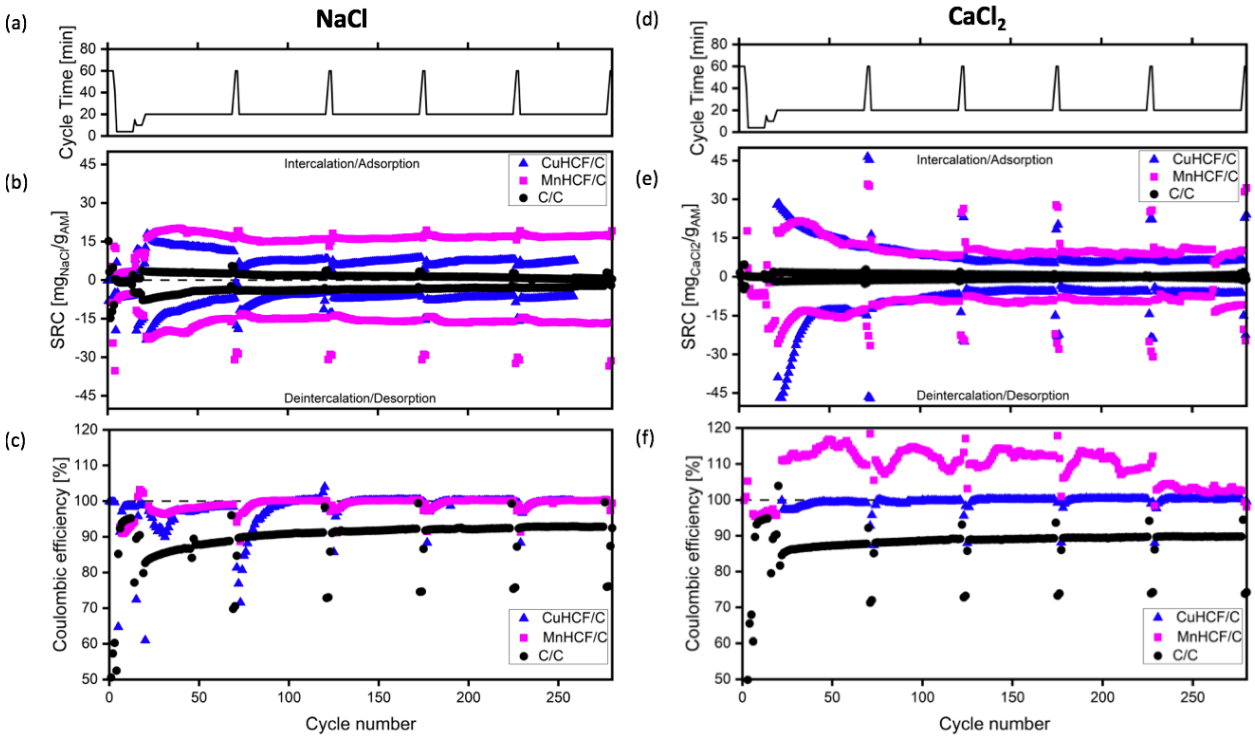

Figure 10. (a,d) Full cycle time (charge and discharge), (b,e) salt removal capacity, and (c,f) Coulombic efficiency as a function of cycle number for each MHCF/C system. Data in panels (a-c) are from tests conducted with NaCl and (d-f) in $CaCl_2$ feed solutions. Positive SRC values correspond to intercalation or adsorption while negative values correspond to deintercalation or desorption. The dashed line in panels (b,e) represent an SRC of 0 while the ones in panels (c,f) correspond to a Coulombic efficiency of 100%.

Figure 10 illustrates the behavior of SRC and Coulombic efficiency as a function of cycle number for MHCF/C and C/C systems tested with NaCl (Figure 10a-c) and $CaCl_2$ (Figure 10d-f) feed solutions. MnHCF/C consistently displays the best SRC when cycled in NaCl (Figure 10b), maintaining its capacity better than CuHCF/C and symmetric C/C for all cycle durations by retaining 83% of its initial SRC after 280 cycles. During the regularly spaced, 30 min capacity check tests, MnHCF SRC values did not increase significantly while CuHCF SRC values decreased. In general, the applied voltage during the longer cycles is not beneficial as it leads to undesirable side reactions as evidenced by decreased Coulombic efficiency in Figure 10c. The SRC for charge cycles in the C/C system became negative over time, a direct result of the inversion effect previously observed in Figure 6a and Figure 7a. Because the C/C cell was shorted during the discharge step, its Coulombic efficiency was consistently lower compared to MHCF/C systems (+1 V applied for discharge), irrespective of feedwater composition. In $CaCl_2$ tests, the SRC values of the MHCF/C systems (Figure 10e) closely mirrored one another until about halfway through the testing protocol when MnHCF/C began to visibly outperform CuHCF/C, which is likely the result of CuHCF dissolution. Generally, longer cycle times increased SRC values in $CaCl_2$, suggesting that the MHCF electrodes had not reached saturation and required longer than 10 min cycles to achieve maximum Ca^{2+} removal from 1000 ppm feed solution. SRC values for 10 min charge cycles

decreased more than those for 30 min cycles for both MHCF/C systems. For MnHCF/C, at the end of the test protocol, the SRC for a 10 min cycle was just 50% that of the initial value while for a 30 min cycle it was 72%. Coulombic efficiency of the CuHCF/C system improved when intercalating Ca^{2+} compared to Na^{+} while it worsened for MnHCF/C, which had values greater than 110% for a majority of the test duration. Values greater than 100% suggest occurrence of side reactions, which in this case were more prominent when a positive potential was applied to the MnHCF electrode for deintercalation.

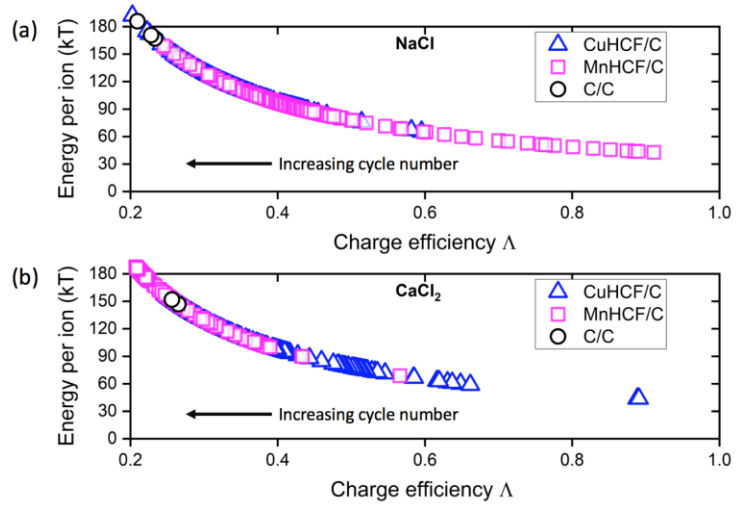

Figure 11. Relationship between charge efficiency Λ and energy consumption per ion (in kT) for C/C, CuHCF/C, and MnHCF/C in (a) NaCl and (b) $CaCl_2$ feedwaters. Each point represents the average energy consumed per ion removed and the charge efficiency for a given charge cycle. Cycles with energy per ion values >180 kT are not displayed. Divide energy in kT/ion by 200 to convert to MJ/mol_{salt}.

Figure 11 shows the energy efficiency for desalination of NaCl and $CaCl_2$ feed solutions with MHCF/C and C/C systems in terms of charge efficiency (the ratio of salt removed to charge transferred) and energy per salt ion removed for a given charge cycle. Although the data for each material follows the same inverse relationship for the two parameters, the position of data points along the curve highlight the differences in energy efficiency of the three systems. In an ideal system, Λ would be 1.0 and all of the current drawn by the cell goes to desalination. However, in experimental systems some of the current goes towards parasitic side reactions like oxygen evolution [9]. Given that such inefficiencies are not accounted for by Coulombic efficiency, which only measures the ratio of charge transferred between charge and discharge cycles, we report the charge efficiency and energy efficiency values for each MHCF/C system. In 1000 ppm NaCl feedwater (Figure 11a), MnHCF/C showed the highest Λ (0.91) and lowest energy consumption (42.6 kT/ion), while CuHCF/C and C/C had lower maximum Λ (0.60, 0.23, respectively) and higher energy consumption (65.4 kT/ion, 167 kT/ion, respectively) due to more energy invested in undesirable side reactions besides desalination. In contrast, in 1000 ppm $CaCl_2$ feedwater (Figure 11b), CuHCF/C removed ions most efficiently (max Λ = 0.89, 43.7 kT/ion) while MnHCF/C (max Λ = 0.57, 68.8 kT/ion) and C/C (max Λ = 0.27, 147 kT/ion) were less energy efficient. Our measured charge efficiency values were lower, and energy consumption values higher, than those previously reported for CDI and mCDI systems [36]. This is likely due to differences in prototype operational parameters used. In general, desalination in constant voltage mode (used in this study) is less efficient than in constant current mode, as it drives more undesirable side reactions [54–57]. Further, we observed performance loss over time, both in terms of higher energy consumption per ion and reduced charge efficiency, when MHCF/C and C/C was cycled in constant voltage mode. This trend can be attributed to the simultaneous decrease in SRR values and preservation of cycle-specific charge transfer as each system ages: under constant

voltage, as the electrode's ability to capture salt decreases, a greater fraction of the current through the cell goes towards side reactions.

Figure S8 shows composite EDS images of carbon electrodes cycled opposite different MHCF electrodes and opposite carbon. The elemental weight ratios corresponding to each image are provided in Table S2. In the pristine sample (Figure S8, left-most), carbon makes up 95% of the electrode and oxygen makes up the rest (5%). The carbon anodes from the symmetric C/C system produce stronger O signals than the pristine sample, suggesting occurrence of carbon surface oxidation as a result of cycling. This is in agreement with the literature, which suggests a more significant O presence in the post-mortem sample as the carbon anode incorporates oxygen containing groups in or on its surface [10]. However, it is not clear why the oxygen levels are higher for the carbon anodes from C/C system tested with NaCl compared to those tested with $CaCl_2$ feed solutions. Of the carbon anodes cycled opposite MHCF electrodes, the anode opposite MnHCF showed the least degradation and had no signs of leachates from MnHCF cathode deposited on it. However, it still had increased amounts of O (10 and 12 wt%), suggestive of carbon oxidation. The lack of Mn atoms on the anode supports the electrochemical data and affirms that MnHCF remains stable throughout cycling, without leaching into the effluent stream. In contrast, for the CuHCF/C and ZnHCF/C systems, significant deposition of cathode constituent elements was observed on the corresponding anodes in addition to the aforementioned increased O levels. On the carbon anode facing CuHCF in NaCl tests, N, Cu, and Fe weight percentages of 21%, 11%, and 5% were measured respectively after cycling. When tested in $CaCl_2$, the carbon anode facing CuHCF showed N, Cu, and Fe weight percentages increase to 26%, 27%, and 12%. Each of these elements are constituents of CuHCF and highlight loss of active material upon cycling. A similar observation was made with the ZnHCF system tested in NaCl, where the carbon anode showed Zn, N, and Fe at 30%, 21%, and 12% by weight, respectively. The observed instability of these materials is in agreement with previous reports of ZnHCF [29] and CuHCF [53]. One approach to improving electrode stability would be minimizing pH fluctuations during cycling, which can be achieved by introducing an ion-selective membrane into the system [50]. Studies have also shown the impact of electrode micro-structure on ion diffusion, highlighting additional opportunities for enhancing system performance[25]. Such system optimization will be the focus of future studies.

4. Conclusions

We successfully prepared, characterized, and tested the desalination performance of intercalation compounds from the $K_xM[Fe(CN)_6]_z \cdot nH_2O$ family (M = Cu, Mn, Zn). Each material was cycled opposite carbon electrodes in a lab-scale prototype device using both 1000 ppm NaCl and 1000 ppm $CaCl_2$ feed solutions. While CuHCF and MnHCF showed promising performance for both Na^+ and Ca^{2+} intercalation, ZnHCF was unstable and underwent rapid dissolution. MnHCF showed the best desalination performance in terms of salt removal capacities (19 mg/g_{AM}) and salt removal rates (4.7 mg/g_{AM}*min) for NaCl while CuHCF showed the best desalination performance in terms of salt removal capacities (46 mg/g_{AM}) and salt removal rates (2.7 mg/g_{AM}*min) for $CaCl_2$. MnHCF proved to be the most robust of the intercalation compounds tested, retaining 83% of its initial capacity after 280 cycles when tested in NaCl and 72% in $CaCl_2$. Further, MnHCF showed no signs of degradation after cycling for 125h in NaCl and $CaCl_2$ feed solutions in our post-mortem analysis of the electrodes. While CuHCF experienced far more dissolution during testing, it was more energy efficient than MnHCF for Ca^{2+} removal; MnHCF was more efficient with Na^+. These results are promising and with electrode and system optimization, the desalination performance of MnHCF and CuHCF materials are likely to be considerably improved. Future work will address such optimization along with testing performance of these electrodes in complex water matrices.

Acknowledgements

We acknowledge support for C.V. Subban and M. J. Schultz-Neu, as well as partial support for prototype development and for E. Sebti from the Laboratory Directed Research and Development Program of Lawrence

Berkeley National Laboratory under U.S. Department of Energy Contract No. DEAC02-05CH11231. The synchrotron experiments reported here were performed at the Stanford Synchrotron Radiation Lightsource (SSRL), a Directorate of SLAC National Accelerator Laboratory and an Office of Science User Facility operated for the U.S. Department of Energy Office of Science by Stanford University. Use of the Stanford Synchrotron Radiation Lightsource, SLAC National Accelerator Laboratory, is supported by the U.S. Department of Energy, Office of Science, Office of Basic Energy Sciences under Contract DE-AC02-76SF00515. Work at the Molecular Foundry was supported by the Office of Science, Office of Basic Energy Sciences, of the U.S. Department of Energy under Contract DE-AC02-05CH11231. The authors would like to thank Joe Wallig for flow cell design and construction, Gary Hubbard for the development of custom control and data acquisition software, and Andreas Backhaus for assistance with test setup optimization.

Author Contributions

Material synthesis was performed by SK, materials characterization by SK, MM, and MMB, electrode fabrication by ES, cyclic voltammetry by JA, prototype design by ES and CVS, desalination performance tests conducted by ES, CVS and MJS, data analysis by ES, MM, and MMB, and post-mortem analysis by ES and SH. All authors contributed to preparation of the manuscript.

References

[1] M.M. Mekonnen, A.Y. Hoekstra, Four billion people facing severe water scarcity, Sci. Adv. 2 (2016) e1500323. https://doi.org/10.1126/sciadv.1500323.
[2] Water scarcity | International Decade for Action “Water for Life” 2005-2015, (2020). https://www.un.org/waterforlifedecade/scarcity.shtml (accessed February 7, 2020).
[3] C.K. Makropoulos, D. Butler, Distributed Water Infrastructure for Sustainable Communities, Water Resour. Manag. 24 (2010) 2795–2816. https://doi.org/10.1007/s11269-010-9580-5.
[4] Y. Oren, Capacitive deionization (CDI) for desalination and water treatment — past, present and future (a review), Desalination. 228 (2008) 10–29. https://doi.org/10.1016/j.desal.2007.08.005.
[5] V.G. Gude, Energy consumption and recovery in reverse osmosis, Desalination Water Treat. 36 (2011) 239–260. https://doi.org/10.5004/dwt.2011.2534.
[6] N.C. Wright, A.G. Winter, Justification for community-scale photovoltaic-powered electrodialysis desalination systems for inland rural villages in India, Desalination. 352 (2014) 82–91. https://doi.org/10.1016/j.desal.2014.07.035.
[7] H. Krishna, INTRODUCTION TO DESALINATION TECHNOLOGIES, (n.d.) 7.
[8] S.-Y. Pan, S.W. Snyder, Y.J. Lin, P.-C. Chiang, Electrokinetic desalination of brackish water and associated challenges in the water and energy nexus, Environ. Sci. Water Res. Technol. 4 (2018) 613–638. https://doi.org/10.1039/C7EW00550D.
[9] B. Shapira, E. Avraham, D. Aurbach, Side Reactions in Capacitive Deionization (CDI) Processes: The Role of Oxygen Reduction, Electrochimica Acta. 220 (2016) 285–295. https://doi.org/10.1016/j.electacta.2016.10.127.
[10] C. Zhang, D. He, J. Ma, W. Tang, T.D. Waite, Faradaic reactions in capacitive deionization (CDI) - problems and possibilities: A review, Water Res. 128 (2018) 314–330. https://doi.org/10.1016/j.watres.2017.10.024.
[11] K. Singh, S. Porada, H.D. de Gier, P.M. Biesheuvel, L.C.P.M. de Smet, Timeline on the application of intercalation materials in Capacitive Deionization, Desalination. 455 (2019) 115–134. https://doi.org/10.1016/j.desal.2018.12.015.
[12] K. Hurlbutt, S. Wheeler, I. Capone, M. Pasta, Prussian Blue Analogs as Battery Materials, Joule. 2 (2018). https://doi.org/10.1016/j.joule.2018.07.017.
[13] H.B. Wu, X.W. (David) Lou, Metal-organic frameworks and their derived materials for electrochemical energy storage and conversion: Promises and challenges, Sci. Adv. 3 (2017) eaap9252. https://doi.org/10.1126/sciadv.aap9252.
[14] B. Wang, Y. Han, X. Wang, N. Bahlawane, H. Pan, M. Yan, Y. Jiang, Prussian Blue Analogs for Rechargeable Batteries, IScience. 3 (2018) 110–133. https://doi.org/10.1016/j.isci.2018.04.008.
[15] H. Kim, J. Hong, K.-Y. Park, H. Kim, S.-W. Kim, K. Kang, Aqueous Rechargeable Li and Na Ion Batteries, Chem. Rev. 114 (2014) 11788–11827. https://doi.org/10.1021/cr500232y.

[16] R.J. Gummow, G. Vamvounis, M.B. Kannan, Y. He, Calcium-Ion Batteries: Current State-of-the-Art and Future Perspectives, Adv. Mater. 30 (2018) 1801702. https://doi.org/10.1002/adma.201801702.
[17] R. Guduru, J. Icaza, A Brief Review on Multivalent Intercalation Batteries with Aqueous Electrolytes, Nanomaterials. 6 (2016) 41. https://doi.org/10.3390/nano6030041.
[18] S. Choi, B. Chang, S. Kim, J. Lee, J. Yoon, J.W. Choi, Battery Electrode Materials with Omnivalent Cation Storage for Fast and Charge-Efficient Ion Removal of Asymmetric Capacitive Deionization, Adv. Funct. Mater. 28 (2018) 1802665. https://doi.org/10.1002/adfm.201802665.
[19] L. Guo, R. Mo, W. Shi, Y. Huang, Z.Y. Leong, M. Ding, F. Chen, H.Y. Yang, A Prussian blue anode for high performance electrochemical deionization promoted by the faradaic mechanism, Nanoscale. 9 (2017) 13305–13312. https://doi.org/10.1039/c7nr03579a.
[20] S. Porada, A. Shrivastava, P. Bukowska, P.M. Biesheuvel, K.C. Smith, Nickel Hexacyanoferrate Electrodes for Continuous Cation Intercalation Desalination of Brackish Water, Electrochimica Acta. 255 (2017) 369–378. https://doi.org/10.1016/j.electacta.2017.09.137.
[21] J. Lee, S. Kim, J. Yoon, Rocking Chair Desalination Battery Based on Prussian Blue Electrodes, Acs Omega. 2 (2017) 1653–1659. https://doi.org/10.1021/acsomega.6b00526.
[22] D.-H. Nam, M.A. Lumley, K.-S. Choi, A Desalination Battery Combining Cu-3[Fe(CN)(6)](2) as a Na-Storage Electrode and Bi as a Cl-Storage Electrode Enabling Membrane-Free Desalination, Chem. Mater. 31 (2019) 1460–1468. https://doi.org/10.1021/acs.chemmater.9b00084.
[23] J. Lee, S. Kim, C. Kim, J. Yoon, Hybrid capacitive deionization to enhance the desalination performance of capacitive techniques, Energy Environ. Sci. 7 (2014) 3683–3689. https://doi.org/10.1039/c4ee02378a.
[24] M. Son, V. Pothanamkandathil, W. Yang, J.S. Vrouwenvelder, C.A. Gorski, B.E. Logan, Improving the Thermodynamic Energy Efficiency of Battery Electrode Deionization Using Flow-Through Electrodes, Environ. Sci. Technol. (2020). https://doi.org/10.1021/acs.est.9b06843.
[25] E.R. Reale, A. Shrivastava, K.C. Smith, Effect of conductive additives on the transport properties of porous flow-through electrodes with insulative particles and their optimization for Faradaic deionization, Water Res. 165 (2019) 114995. https://doi.org/10.1016/j.watres.2019.114995.
[26] R. Chen, H. Tanaka, T. Kawamoto, M. Asai, C. Fukushima, H. Na, M. Kurihara, M. Watanabe, M. Arisaka, T. Nankawa, Selective removal of cesium ions from wastewater using copper hexacyanoferrate nanofilms in an electrochemical system, Electrochimica Acta. 87 (2013) 119–125. https://doi.org/10.1016/j.electacta.2012.08.124.
[27] T. Kim, C.A. Gorski, B.E. Logan, Low Energy Desalination Using Battery Electrode Deionization, Environ. Sci. Technol. Lett. 4 (2017) 444–449. https://doi.org/10.1021/acs.estlett.7b00392.
[28] L. Zhang, L. Chen, X. Zhou, Z. Liu, Morphology-Dependent Electrochemical Performance of Zinc Hexacyanoferrate Cathode for Zinc-Ion Battery, Sci. Rep. 5 (2015) 18263. https://doi.org/10.1038/srep18263.
[29] L. Zhang, L. Chen, X. Zhou, Z. Liu, Towards High-Voltage Aqueous Metal-Ion Batteries Beyond 1.5 V: The Zinc/Zinc Hexacyanoferrate System, Adv. Energy Mater. 5 (2015) 1400930. https://doi.org/10.1002/aenm.201400930.
[30] X. Zhu, W. Xu, G. Tan, Y. Wang, Concentration Flow Cells for Efficient Salinity Gradient Energy Recovery with Nanostructured Open Framework Hexacyanoferrate Electrodes, ChemistrySelect. 3 (2018) 5571–5580. https://doi.org/10.1002/slct.201800312.
[31] A. Shrivastava, S. Liu, K. C. Smith, Linking capacity loss and retention of nickel hexacyanoferrate to a two-site intercalation mechanism for aqueous Mg 2+ and Ca 2+ ions, Phys. Chem. Chem. Phys. 21 (2019) 20177–20188. https://doi.org/10.1039/C9CP04115J.
[32] K. Singh, Z. Qian, P.M. Biesheuvel, H. Zuilhof, S. Porada, L.C.P.M. de Smet, Nickel hexacyanoferrate electrodes for high mono/divalent ion-selectivity in capacitive deionization, Desalination. 481 (2020) 114346. https://doi.org/10.1016/j.desal.2020.114346.
[33] R.Y. Wang, C.D. Wessells, R.A. Huggins, Y. Cui, Highly Reversible Open Framework Nanoscale Electrodes for Divalent Ion Batteries, Nano Lett. 13 (2013) 5748–5752. https://doi.org/10.1021/nl403669a.
[34] J.J. Urban, Emerging Scientific and Engineering Opportunities within the Water-Energy Nexus, Joule. 1 (2017) 665–688. https://doi.org/10.1016/j.joule.2017.10.002.
[35] X. Bie, K. Kubota, T. Hosaka, K. Chihara, S. Komaba, Synthesis and electrochemical properties of Na-rich Prussian blue analogues containing Mn, Fe, Co, and Fe for Na-ion batteries, J. Power Sources. 378 (2018) 322–330. https://doi.org/10.1016/j.jpowsour.2017.12.052.

[36] M.E. Suss, S. Porada, X. Sun, P.M. Biesheuvel, J. Yoon, V. Presser, Water desalination via capacitive deionization: What is it and what can we expect from it?, Energy Environ. Sci. 8 (2015) 2296–2319. https://doi.org/10.1039/c5ee00519a.
[37] D.O. Ojwang, J. Grins, D. Wardecki, M. Valvo, V. Renman, L. Häggström, T. Ericsson, T. Gustafsson, A. Mahmoud, R.P. Hermann, G. Svensson, Structure Characterization and Properties of K-Containing Copper Hexacyanoferrate, Inorg. Chem. 55 (2016) 5924–5934. https://doi.org/10.1021/acs.inorgchem.6b00227.
[38] V. Jassal, U. Shanker1, Synthesis, Characterization and Applications of Nano-structured Metal Hexacyanoferrates: A Review, J. Environ. Anal. Chem. 02 (2015). https://doi.org/10.4172/2380-2391.1000128.
[39] J.W. Smith, R.J. Saykally, Soft X-ray Absorption Spectroscopy of Liquids and Solutions, Chem. Rev. 117 (2017) 13909–13934. https://doi.org/10.1021/acs.chemrev.7b00213.
[40] F. Lin, Y. Liu, X. Yu, L. Cheng, A. Singer, O.G. Shpyrko, H.L. Xin, N. Tamura, C. Tian, T.-C. Weng, X.-Q. Yang, Y.S. Meng, D. Nordlund, W. Yang, M.M. Doeff, Synchrotron X-ray Analytical Techniques for Studying Materials Electrochemistry in Rechargeable Batteries, Chem. Rev. 117 (2017) 13123–13186. https://doi.org/10.1021/acs.chemrev.7b00007.
[41] W.-S. Yoon, O. Haas, S. Muhammad, H. Kim, W. Lee, D. Kim, D.A. Fischer, C. Jaye, X.-Q. Yang, M. Balasubramanian, K.-W. Nam, In situ soft XAS study on nickel-based layered cathode material at elevated temperatures: A novel approach to study thermal stability, Sci. Rep. 4 (2014) 6827. https://doi.org/10.1038/srep06827.
[42] J. van Elp, G. Peng, B.G. Searle, S. Mitra-Kirtley, Y.H. Huang, M.K. Johnson, Z.H. Zhou, M.W.W. Adams, M.J. Maroney, S.P. Cramer, Electronic Structure and Symmetry in Nickel L Edge X-ray Absorption Spectroscopy: Application to a Nickel Protein, J. Am. Chem. Soc. 116 (1994) 1918–1923. https://doi.org/10.1021/ja00084a036.
[43] R.K. Hocking, E.C. Wasinger, F.M.F. de Groot, K.O. Hodgson, B. Hedman, E.I. Solomon, Fe L-Edge XAS Studies of K4[Fe(CN)6] and K3[Fe(CN)6]: A Direct Probe of Back-Bonding, J. Am. Chem. Soc. 128 (2006) 10442–10451. https://doi.org/10.1021/ja061802i.
[44] M. Risch, K.A. Stoerzinger, T.Z. Regier, D. Peak, S.Y. Sayed, Y. Shao-Horn, Reversibility of Ferri-/Ferrocyanide Redox during Operando Soft X-ray Spectroscopy, J. Phys. Chem. C. 119 (2015) 18903–18910. https://doi.org/10.1021/acs.jpcc.5b04609.
[45] Y. Bouhadana, E. Avraham, M. Noked, M. Ben-Tzion, A. Soffer, D. Aurbach, Capacitive Deionization of NaCl Solutions at Non-Steady-State Conditions: Inversion Functionality of the Carbon Electrodes, J. Phys. Chem. C. 115 (2011) 16567–16573. https://doi.org/10.1021/jp2047486.
[46] Y. Bouhadana, M. Ben-Tzion, A. Soffer, D. Aurbach, A control system for operating and investigating reactors: The demonstration of parasitic reactions in the water desalination by capacitive de-ionization, Desalination. 268 (2011) 253–261. https://doi.org/10.1016/j.desal.2010.10.037.
[47] D. He, C.E. Wong, W. Tang, P. Kovalsky, T.D. Waite, Faradaic Reactions in Water Desalination by Batch-Mode Capacitive Deionization, Environ. Sci. Technol. Lett. 3 (2016) 222–226. https://doi.org/10.1021/acs.estlett.6b00124.
[48] T. Kim, J. Yu, C. Kim, J. Yoon, Hydrogen peroxide generation in flow-mode capacitive deionization, J. Electroanal. Chem. 776 (2016) 101–104. https://doi.org/10.1016/j.jelechem.2016.07.001.
[49] I. Cohen, E. Avraham, Y. Bouhadana, A. Soffer, D. Aurbach, Long term stability of capacitive de-ionization processes for water desalination: The challenge of positive electrodes corrosion, Electrochimica Acta. 106 (2013) 91–100. https://doi.org/10.1016/j.electacta.2013.05.029.
[50] J. Yu, K. Jo, T. Kim, J. Lee, J. Yoon, Temporal and spatial distribution of pH in flow-mode capacitive deionization and membrane capacitive deionization, Desalination. 439 (2018) 188–195. https://doi.org/10.1016/j.desal.2018.04.011.
[51] S. Shanbhag, J.F. Whitacre, M.S. Mauter, The Origins of Low Efficiency in Electrochemical De-Ionization Systems, J. Electrochem. Soc. 163 (2016) E363–E371. https://doi.org/10.1149/2.0181614jes.
[52] J.E. Dykstra, K.J. Keesman, P.M. Biesheuvel, A. van der Wal, Theory of pH changes in water desalination by capacitive deionization, Water Res. 119 (2017) 178–186. https://doi.org/10.1016/j.watres.2017.04.039.
[53] T. Kim, C.A. Gorski, B.E. Logan, Ammonium removal from domestic wastewater using selective battery electrodes, Environ. Sci. Technol. Lett. 5 (2018) 578–583. https://doi.org/10.1021/acs.estlett.8b00334.
[54] R. Zhao, P.M. Biesheuvel, A. van der Wal, Energy consumption and constant current operation in membrane capacitive deionization, Energy Environ. Sci. 5 (2012) 9520. https://doi.org/10.1039/c2ee21737f.

[55] J. Kang, T. Kim, K. Jo, J. Yoon, Comparison of salt adsorption capacity and energy consumption between constant current and constant voltage operation in capacitive deionization, Desalination. 352 (2014) 52–57. https://doi.org/10.1016/j.desal.2014.08.009.
[56] Y. Qu, P.G. Campbell, L. Gu, J.M. Knipe, E. Dzenitis, J.G. Santiago, M. Stadermann, Energy consumption analysis of constant voltage and constant current operations in capacitive deionization, Desalination. 400 (2016) 18–24. https://doi.org/10.1016/j.desal.2016.09.014.
[57] L. Han, K.G. Karthikeyan, K.B. Gregory, Energy Consumption and Recovery in Capacitive Deionization Using Nanoporous Activated Carbon Electrodes, J. Electrochem. Soc. 162 (2015) E282–E288. https://doi.org/10.1149/2.0431512jes.